

The effect of defect size on the quantitative estimation of defect depth using sonic infrared imaging

Cite as: Rev. Sci. Instrum. 90, 054902 (2019); doi: 10.1063/1.5078380

Submitted: 24 October 2018 • Accepted: 1 May 2019 •

Published Online: 22 May 2019



View Online



Export Citation



CrossMark

Omar Obeidat,^{1,a)}  Qiuye Yu,¹ Lawrence Favro,² and Xiaoyan Han¹

AFFILIATIONS

¹Department of Electrical and Computer Engineering, Wayne State University, Detroit, Michigan 48202, USA

²Physics and Astronomy, Wayne State University, Detroit, Michigan 48202, USA

^{a)}Email: fj9807@wayne.edu.

ABSTRACT

Sonic infrared (SIR) imaging is a hybrid nondestructive evaluation (NDE) method that uses ultrasonic excitation along with thermal imaging to detect defects in materials and structures. SIR NDE uses an ultrasonic pulse in the 15–40 kHz range from a transducer to produce localized heating at the defect while a thermal camera will record surface temperature during the inspection. In a previous article, we presented a model that describes heat diffusion from subsurface defects in a composite material. The model uses certain aspects of the temperature-time curve for defect depth profiling, namely, half-maximum power time, the peak slope time, and the second derivative peak time. In this study, we investigate the effect of defect size on the quantitative estimation of defect depth. The theoretical results are calculated and compared with the experimental data. We demonstrate that the experimental data have good correlation with the theoretical calculation. The peak slope time and the second derivative peak time are less sensitive to changes in defect size than the half-maximum power time in the defect depth assessment.

Published under license by AIP Publishing. <https://doi.org/10.1063/1.5078380>

I. INTRODUCTION

Sonic infrared (SIR) is a hybrid nondestructive evaluation (NDE) method that uses ultrasonic excitation along with thermal imaging to detect defects in materials and structures.^{1,2} SIR NDE uses an ultrasonic pulse in the 15–40 kHz range to produce localized heating at the defect while a thermal camera will observe surface temperature during the inspection. The captured images are in 12-bit gray scale where the pixels' intensities are functions of their corresponding surface temperatures. The thermal camera is synchronized to begin acquiring frames just before the launch of the ultrasonic pulse and to continue capturing frames for a desired length of time. Once the ultrasonic pulse is applied, different heating mechanisms contribute to heat generation process causing the defect area to be heated; defects are recognized as bright spots on a dark background.^{3–8} SIR NDE can detect surface and subsurface defects in a wide variety of materials such as metals, metal alloys, and composites. So far, it is found that the technique is not very sensitive to crack geometry or orientation. It is deployed in many practical applications such as inspecting

massive automobile parts,⁹ civil structures assurance,¹⁰ and air craft structures.^{11–14}

Composites have become genuine components in modern aircraft and aerospace designs. They are desired due to their light weight, high strength, high specific stiffness and design flexibility. However, impact damage is often a common problem for modern composite structures; considerable internal damage can occur at any depth without any indication on the surface. Defect depth quantification is of paramount importance in quantitative NDE; precise depth estimation can aid repair assessments and reduce maintenance costs. Subsurface defects can be modelled as local heat sources. Temperature distribution induced by instantaneous planar heat sources in orthotropic materials is presented in Ref. 15. In lock-in vibrothermography, phase information is used to retrieve defects depth.^{16,17} Theoretical models of surface temperature caused by subsurface defects with various orientations in isotropic materials are presented in Refs. 18 and 19. In SIR, Ouyang presented a model to describe the thermosonic imaging of subsurface rectangular cracks.²⁰ Zhao *et al.* attempted to profile depths of defects in composites in Ref. 21. In Ref. 22, we introduced a

theoretical model for a circular subsurface heat source of duration τ in a composite. In addition to material properties, the model also considers defect depth, size, and the duration of ultrasonic excitation. Defect size contributes to the detectability of defects as well as depth quantification. The effect of defect size on the quantitative estimation of defects in pulsed thermography²³ and lock-in thermography²⁴ was investigated. In this article, the investigation on the effect of defect size for quantitative flaw characterization is presented.

II. THEORY

The model describes the surface temperature $T(0, t)$ at time t induced by a subsurface circular heat source of radius (R) and heating duration (τ) located at a depth (d) in a composite panel of total thickness (L). The composite has density (ρ) and average heat capacity (c). It is assumed here that the material has uniform thermal diffusivity in the plane of the panel (i.e., $\alpha_x = \alpha_y$) and thermal diffusivity α_z in the plane out of the panel. The surface temperature of the point that coincides with the defect center is given by Ref. 22,

$$T(\vec{0}, t) = \begin{cases} a \sum_{n=-\infty}^{\infty} \sqrt{t} \exp(-B^2/t) - \sqrt{\pi} B \cdot \operatorname{erfc}\left(\frac{B}{\sqrt{t}}\right) - a \sum_{n=-\infty}^{\infty} \sqrt{t} \exp(-C^2/t) - \sqrt{\pi} C \cdot \operatorname{erfc}\left(\frac{C}{\sqrt{t}}\right) & t \leq \tau \\ a \sum_{n=-\infty}^{\infty} \sqrt{t} \exp(-B^2/t) - \sqrt{t-\tau} \exp(-B^2/(t-\tau)) + B\sqrt{\pi} \left(\operatorname{erfc}\left(\frac{B}{\sqrt{t-\tau}}\right) - \operatorname{erfc}\left(\frac{B}{\sqrt{t}}\right) \right) \\ - a \sum_{n=-\infty}^{\infty} \sqrt{t} \exp(-C^2/t) - \sqrt{t-\tau} \exp(-C^2/(t-\tau)) + C\sqrt{\pi} \left(\operatorname{erfc}\left(\frac{C}{\sqrt{t-\tau}}\right) - \operatorname{erfc}\left(\frac{C}{\sqrt{t}}\right) \right) & t > \tau \end{cases}, \quad (1)$$

where

$$a = \frac{1}{\rho c (\pi \alpha_z)^{1/2}}, \quad (2)$$

$$B = \sqrt{\frac{(d - 2nL)^2}{4\alpha_z}}, \quad (3)$$

$$C = \sqrt{\frac{(d - 2nL)^2}{4\alpha_z} + \frac{R^2}{4\alpha_x}}, \quad (4)$$

$$\operatorname{erfc}(x) = \frac{2}{\sqrt{\pi}} \int_x^{\infty} e^{-t^2} dt. \quad (5)$$

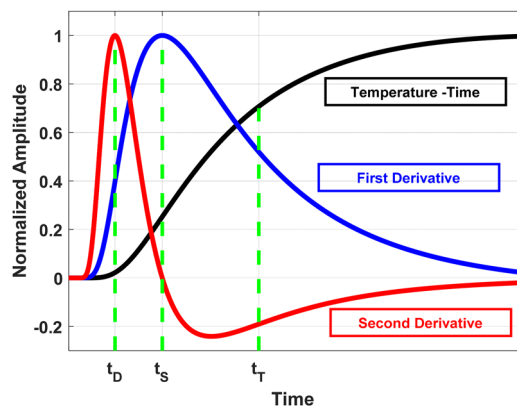


FIG. 1. Illustrative sketch of a temperature-time curve, first derivative curve, and the second derivative curves with the features used for depth profiling in SIR as marked, t_T , t_S , and t_D .

Three features in the temperature-time curve are used for depth profiling:

1. Half-maximum power time t_T : this is the time at which the temperature curve reaches half of its maximum power or is $1/\sqrt{2}$ of its peak temperature.
2. Peak slope time t_S : the time at which the 1st derivative, or the slope, of the temperature-time data reaches the maximum.
3. Second derivative peak time t_D : the time at which the second derivative of the temperature-time data reaches the maximum.

The illustrative sketch of a temperature-time curve and its derivatives are shown in Fig. 1 below. The features used for depth profiling are indicated in the sketch as well, t_T , t_S , and t_D . It can be shown that a linear relationship between the depth squared and any of these features can be established and used for depth profiling.²²

The model in (1) suggests that defect size contributes to the total temperature-time curve. Below, we present and discuss the analytical results of the above-mentioned features for different defect sizes at different depths.

III. THEORETICAL MODELING RESULTS

The analytical model suggests that the defect size affects the characterization of the subsurface defects. The set of theoretical results of the half-maximum power time, peak slope time, and the second derivative peak time for the defects of different sizes located at different depths is computed based on the analytical model in (1). It is assumed that the structure material is isotropic with thermal diffusivity $\alpha = 0.21 \text{ mm}^2/\text{s}$. Since the material is isotropic, Eqs. (2)–(4) will be modified such that

TABLE I. Defects' depths used for analytical modeling.

Index number of defect depth	Depth (mm)
1	1.17
2	1.68
3	2.08
4	2.61
5	3.18
6	3.63
7	4.11
8	4.62

TABLE II. Defects' sizes used for analytical modeling.

Defect name	Size (mm)
R1	19.05
R2	15.88
R3	12.70
R4	9.53
R5	6.35

$$a = \frac{1}{\rho c (\pi \alpha)^{1/2}}, \quad (2')$$

$$B = \sqrt{\frac{(d - 2nL)^2}{4\alpha}}, \quad (3')$$

$$C = \sqrt{\frac{(d - 2nL)^2 + R^2}{4\alpha}}. \quad (4')$$

The depths of defects are listed in Table I, and the defects sizes (radii) are listed in Table II. The duration of ultrasonic excitation τ is 5 ms. Since temporal information is of the only interest in this article, all the temperature-time curves are normalized. The features of interest are calculated and presented in Tables III–V, respectively.

The theoretical results in Table III show that the defect size has no significant effect on the half maximum power time for near surface defects. As the defect depth increases (i.e., greater than 2.61 mm), the differences become more apparent; larger defect sizes will have significantly higher half-maximum power time. On the other hand, the peak slope time in Table IV is less sensitive to changes in defect size; the peak slope time for different defect sizes has not changed except for R5 for defects at depths 3.63, 4.11, and 4.62 mm, respectively. The second derivative peak time shown

TABLE III. Theoretical results of half-maximum power time for different defect sizes.

Index number of defect depth	Depth (mm)	Half-maximum power time (s)				
		R1	R2	R3	R4	R5
1	1.17	1.27	1.27	1.27	1.27	1.27
2	1.68	2.61	2.61	2.61	2.61	2.59
3	2.08	4.00	4.00	4.00	3.99	3.89
4	2.61	6.35	6.35	6.34	6.28	5.90
5	3.18	9.35	9.35	9.3	9.07	8.16
6	3.63	12.18	12.15	12.02	11.54	10.08
7	4.11	15.59	15.5	15.21	14.33	12.22
8	4.62	19.64	19.44	18.87	17.43	16.42

TABLE IV. Theoretical results of peak slope time for different defect sizes.

Index number of defect depth	Depth (mm)	Peak slope time (s)				
		R1	R2	R3	R4	R5
1	1.17	0.60	0.60	0.60	0.60	0.60
2	1.68	1.24	1.24	1.24	1.24	1.24
3	2.08	1.89	1.89	1.89	1.89	1.89
4	2.61	3.00	3.00	3.00	3.00	3.00
5	3.18	4.42	4.42	4.42	4.42	4.42
6	3.63	5.76	5.76	5.76	5.76	5.74
7	4.11	7.38	7.38	7.38	7.38	7.29
8	4.62	9.33	9.33	9.33	9.33	9.05

TABLE V. Theoretical results of second derivative peak time for different defect sizes.

Index number of defect depth	Depth (mm)	Second derivative peak time (s)				
		R1	R2	R3	R4	R5
1	1.17	0.30	0.30	0.30	0.30	0.30
2	1.68	0.61	0.61	0.61	0.61	0.61
3	2.08	0.93	0.93	0.93	0.93	0.93
4	2.61	1.48	1.48	1.48	1.48	1.48
5	3.18	2.18	2.18	2.18	2.18	2.18
6	3.63	2.84	2.84	2.84	2.84	2.84
7	4.11	3.64	3.64	3.64	3.64	3.64
8	4.62	4.60	4.60	4.60	4.60	4.60

in Table V is the same for all defect sizes over the total range of defects in the table. The effect of lateral heat diffusion on the defect-center temperature is at minimum at the early stages.

IV. EXPERIMENTAL ARRANGEMENT AND SAMPLE

To investigate the effect of defect size on depth profiling, experiments were designed such that the features of interest are collected

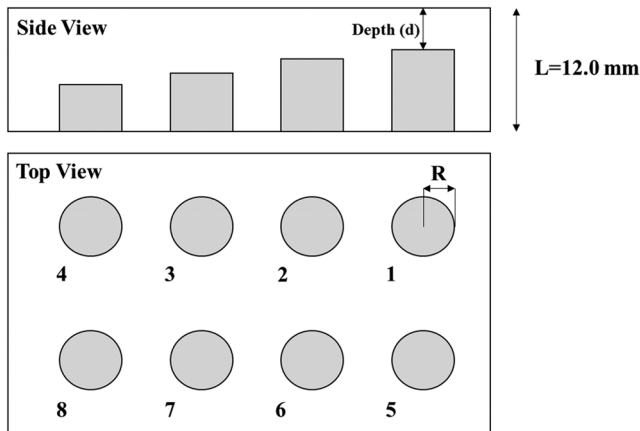


FIG. 2. Schematic diagram of a plastic sample having eight back-milled flat-bottomed holes of the same size at different depths beneath the front surface.

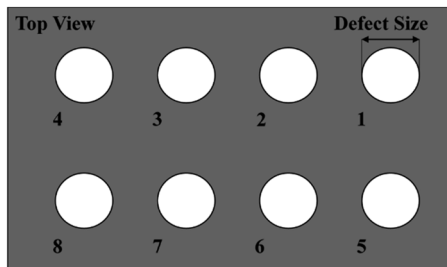


FIG. 3. Top view of the thermal mask used to control defects' heating.

over a range of defect depths and sizes. The material chosen was a DELRIN panel of length 30.6 cm, breadth 16 cm, and thickness 1.2 cm. It is a hard-plastic material, isotropic with diffusivity of $0.21 \text{ mm}^2/\text{s}$. Flat-bottom holes of defects with radius of 19.05 mm

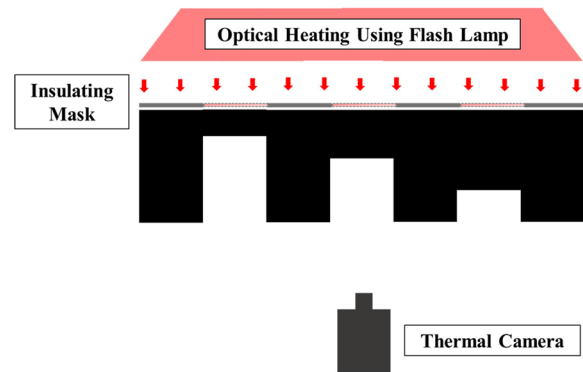


FIG. 4. Sketch of the experimental setup.

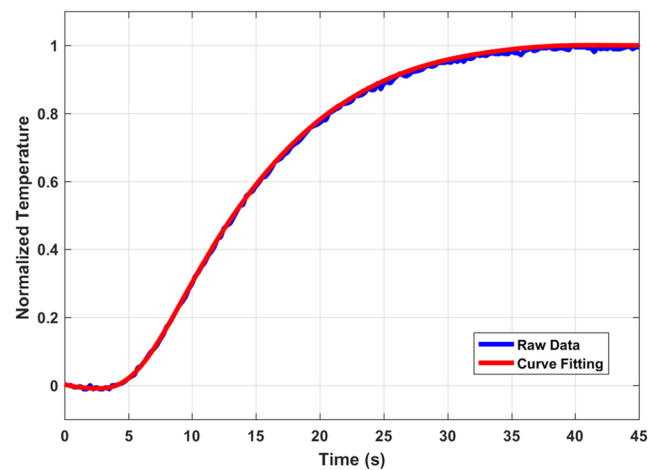


FIG. 5. Theoretical vs experimental temperature-time curves and their derivatives for an artificial heat source of radius 9.53 mm located at depth 4.62 mm.

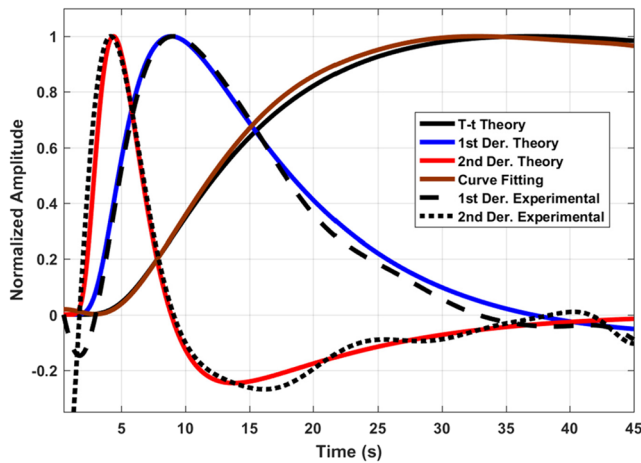


FIG. 6. Theoretical vs experimental temperature-time curves and their derivatives for an artificial heat source of radius 9.53 mm located at depth 4.62 mm.

at different depths were machined as depicted in Fig. 2. The depths of defects listed in Table I for theoretical modeling are the same with these flat-bottom holes in this sample. The conducted experiments simulate subsurface defects by using a combination of optical heat

source and an insulating mask; a set of two flash lamps were used to provide a uniform spatial heating profile with heating duration (τ) of 5 ms. The total energy of the flash light was 6 kJ. However, a portion of the generated heat is used to illuminate the holes as the remaining part was blocked by a mask. Defects' sizes are controlled using insulating masks of different opening sizes; openings have radii of 19.05, 15.88, 12.70, 9.53, and 6.35 mm. The used masks are flat masks, which are attached to the flat surface of the sample. The masks are made of thick cardboard with good insulation properties. The masks were attached to the flash opening and were illuminated during the experiment, a top view of the mask is shown in Fig. 3. The flash along with the mask can act as a secondary heat source, which may affect the accuracy of the results, so they were removed immediately after it was lunched. The experimental setup mimics subsurface defects with depths equal to the holes' thicknesses. A thermal camera is used to observe the heat on the flat side of the plate. The camera is a focal plane array-based forward-looking infrared (FLIR) onboard cooled camera with spatial resolution of 640×512 pixels. The temperature resolution of the camera is 20 mK at the standard condition; its maximum frame rate at full window is 120 fps. The frame rate used in the experiment is 10 fps. Figure 4 shows the experimental setup.

V. EXPERIMENTAL RESULTS

The thermal image sequences collected during the inspections were used to construct temperature-time curves of the defect

TABLE VI. Experimental results of half maximum power time for different defect sizes.

Index number of defect depth	Depth (mm)	Half-maximum power time (s)				
		R1	R2	R3	R4	R5
1	1.17	1.26	1.31	1.3	1.29	1.18
2	1.68	2.55	2.64	2.63	2.62	2.34
3	2.08	4.30	4.46	4.44	4.38	3.81
4	2.61	6.49	6.62	6.56	6.50	5.48
5	3.18	9.05	9.69	9.31	9.08	7.82
6	3.63	12.04	12.74	12.1	11.79	9.87
7	4.11	15.32	15.96	15.31	14.86	12.19
8	4.62	19.22	20.06	18.55	18.11	14.91

TABLE VII. Experimental results of first derivative peak time for different defect sizes.

Index number of defect depth	Depth (mm)	First derivative peak time (s)				
		R1	R2	R3	R4	R5
1	1.17	0.6	0.64	0.64	0.63	0.61
2	1.68	1.25	1.27	1.31	1.27	1.2
3	2.08	2.07	2.11	2.17	2.14	2.12
4	2.61	3.20	3.23	3.2	3.23	2.88
5	3.18	4.51	4.48	4.65	4.57	4.32
6	3.63	5.95	6.2	6.05	5.98	5.66
7	4.11	7.77	7.81	7.74	7.85	7.35
8	4.62	9.46	9.79	9.46	9.65	8.95

TABLE VIII. Experimental results of second derivative peak time for different defect sizes.

Index number of defect depth	Depth (mm)	Second derivative peak time (s)				
		R1	R2	R3	R4	R5
1	1.17	0.28	0.28	0.26	0.26	0.26
2	1.68	0.56	0.55	0.53	0.57	0.62
3	2.08	0.99	1.00	0.92	0.95	0.92
4	2.61	1.43	1.51	1.49	1.5	1.43
5	3.18	2.14	2.23	2.13	2.2	2.15
6	3.63	2.83	2.83	2.85	2.84	3.04
7	4.11	3.68	3.68	3.75	3.55	3.73
8	4.62	4.74	4.60	4.55	4.55	4.66

signature at the surface. The constructed curves were smoothed using a high-order polynomial fitting; polynomial curve fitting also facilitates analytical differentiation. The polynomial coefficients resulted from the fitting process are used to plot the “fitted function” using a step of 0.01 s and thus temporal resolution is improved. Figure 5 shows the normalized raw data vs the normalized fitted curve; the polynomial order used was 15, and the coefficient of determination $R^2 = 0.999$.

Figure 6 shows the normalized theoretical temperature-time curve vs the normalized experimental temperature curve and their derivatives for heat source of radius 9.53 mm located at depths of 4.62 mm. Estimated half-maximum time, peak slope time, and the second derivative peak time for five defect sizes are listed in Tables VI–VIII, respectively. The tables show the experimental results for the features of interest for different defect sizes at different depths.

VI. DISCUSSION

Comparisons between the theoretical modeling and experimental results are presented in Figs. 7–9. Figure 7 is for the

half-maximum power time for five defect sizes located at different depths; Fig. 8 is for the peak slope time for five defect sizes located at different depths; and Fig. 9 is for the second derivative peak time for five defect sizes located at different depths. In all of three figures, the theoretical data are represented by squares of different colors while the experimental data are presented by red circles in the three figures.

From Fig. 7, one can see that the experimental data come in fine agreement with the theoretical modeling. As the analytical model suggests, while the defect is near the surface, the defect size does not change the half-maximum power time. However, as the defect depth increases, the effect of defect size will become more noticeable.

The peak slope time appears earlier in the temperature-time curve with lower signal level. From Fig. 8, the theoretical data suggests that the first derivative peak time is less sensitive to changes in defect size compared to the half-maximum power time.

The second derivative peak time is the first feature to appear in the temperature-time curve with minimum signal level. Although

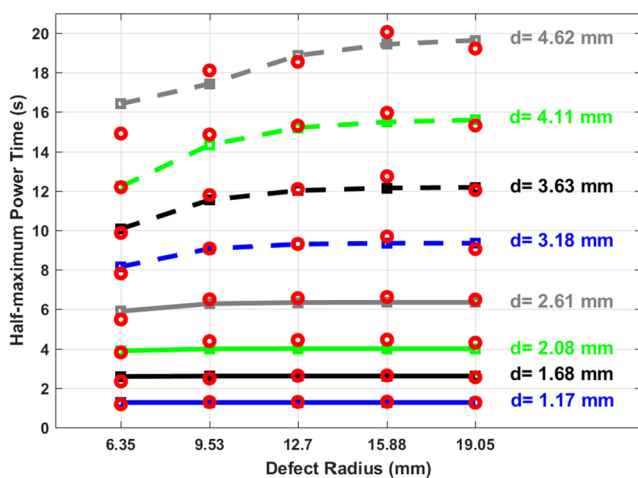


FIG. 7. Half-maximum power time for defects of different sizes located at various depths, the experimental data are represented by red circles.

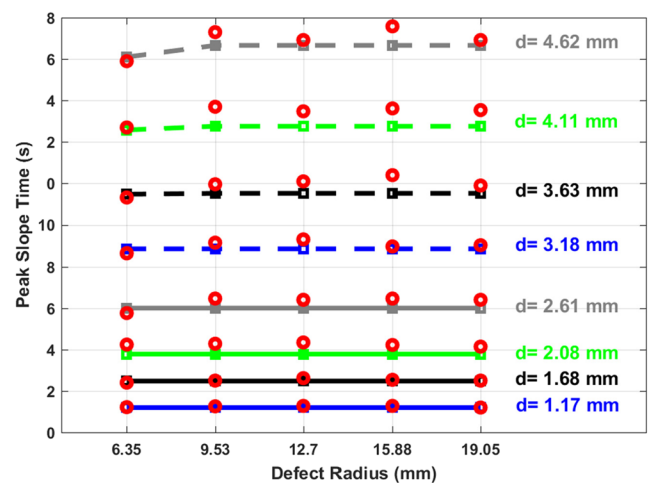


FIG. 8. First derivative peak time for defects of different sizes located at various depths, the experimental data are represented by red circles.

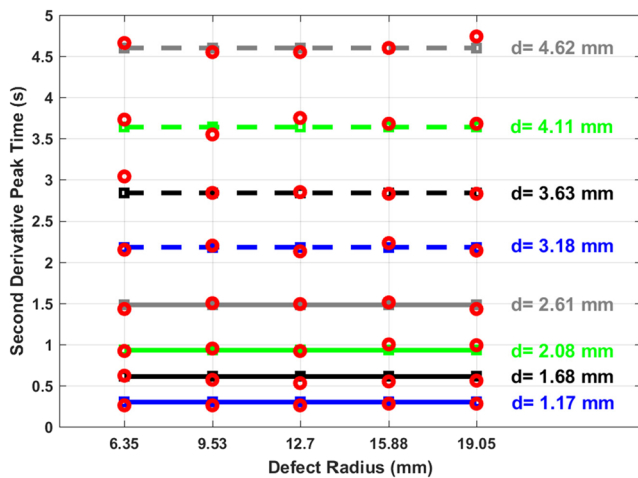


FIG. 9. Second derivative peak time for defects of different sizes located at various depths, the experimental data are represented by red circles.

quantitative estimation of this feature is more prone to error due to its low signal-to-noise ratio (SNR), it is the least sensitive parameter to the changes in defect size, as lateral heat diffusion effect at early time is at minimum compared with the other two features, as shown in Fig. 9.

It is worth mentioning that typical sonic IR inspections will have undesired heat sources including bulk heating and mode pattern. Bulk heating arises due to ultrasound wave attenuation in the structure while mode patterns result from standing waves established during the inspection. Bulk heating will be significant near the ultrasonic transducer where the applied ultrasonic wave is still at its maximum; as the ultrasonic wave propagates away from the sample it will attenuate, and the bulk heating will decrease gradually. However, it is valid to assume that bulk heating will be uniform in the local domain; the differences in bulk heating for areas that have the same distance from the ultrasonic source are insignificant. Mode patterns are a concern for SIR NDE practitioners as they often cause problems in defect identification and characterization. However, by applying chaotic excitation (i.e., multifrequency sound excitation) instead of monochromatic excitation, background heat patterns can be greatly reduced since mode patterns tend to be averaged out.

VII. CONCLUSION

The effect of defect size on defect characterization in SIR NDE was investigated. As the defect is near the surface, defect size has negligible effect in defect characterization. For deeper defects, half-maximum power is affected significantly by changes in defect size,

the second derivative peak time is the least sensitive parameter to the changes in defect size. When signal to noise ratio is low, peak slope time can be used as an alternative parameter to identify defect depth for optimized results.

ACKNOWLEDGMENTS

This work was sponsored by Wayne State University.

REFERENCES

- ¹L. D. Favro, X. Han, Z. Ouyang, G. Sun, H. Sui, and R. L. Thomas, *Rev. Sci. Instrum.* **71**(6), 2418 (2000).
- ²X. Han, "Sonic infrared imaging: A novel NDE technology for detection of cracks/delaminations/disbonds in materials and structures," in *Ultrasonic and Advanced Methods for Nondestructive Testing and Material Characterization* (World Scientific, 2007), p. 369.
- ³J. Renshaw, J. C. Chen, S. D. Holland, and R. Bruce Thompson, *NDT&E Int.* **44**(8), 736 (2011).
- ⁴J. C. Chen, K. Jacob, K. Lick, and W. T. Riddell, *Nondestruct. Test. Eval.* **22**(2-3), 83 (2007).
- ⁵K. L. Reifsnider, E. G. Henneke, and W. W. Stinchcomb, "The mechanics of vibrothermography," in *Mechanics of Nondestructive Testing* (Springer, 1980), p. 249.
- ⁶R. Montanini and F. Freni, *NDT&E Int.* **58**, 43 (2013).
- ⁷O. Obeidat, Q. Yu, and X. Han, *Sens. Imaging* **17**(1), 22 (2016).
- ⁸Q. Yu, O. Obeidat, and X. Han, "Ultrasound wave excitation in thermal NDE for defect detection," *NDT&E Int.* **100**, 153 (2018).
- ⁹X. Han, L. D. Favro, Z. Ouyang, and R. L. Thomas, *AIP Conf. Proc.* **615**(1), 552 (2002).
- ¹⁰Q. He and X. Han, *AIP Conf. Proc.* **1430**(1), 540 (2012).
- ¹¹X. Han, J. Lu, M. S. Islam, W. Li, Z. Zeng, N. Kashyap, E. Yitamben, L. D. Favro, G. M. Newaz, and R. L. Thomas, *AIP Conf. Proc.* **760**(1), 632 (2005).
- ¹²X. Han, S. Zhao, D. Zhang, A. Lubowicki, L. Favro, R. Thomas, and G. Newaz, in *Proceedings of 11th Quantitative InfraRed Thermography Conference* (2012), paper QIRT2012-185, p. 11.
- ¹³A. Mian, X. Han, S. Islam, and G. Newaz, *Compos. Sci. Technol.* **64**(5), 657 (2004).
- ¹⁴X. Han, L. D. Favro, and R. L. Thomas, *J. Phys. D: Appl. Phys.* **44**(3), 034013 (2010).
- ¹⁵R. L. Thomas *et al.*, "Thermal methods used in composite inspection," *Compr. Compos. Mater.* **5**, 427 (2000).
- ¹⁶T. Zweschper, A. Dillenz, and G. Busse, *Insight* **43**, 173 (2001).
- ¹⁷R. Montanini, F. Freni, and G. L. Rossi, *Rev. Sci. Instrum.* **83**(9), 094902 (2012).
- ¹⁸A. Mendioroz, E. Apiñaniz, A. Salazar, P. Venegas, and I. Sáez-Ocáriz, *J. Phys. D: Appl. Phys.* **42**(5), 055502 (2009).
- ¹⁹A. Salazar, A. Mendioroz, E. Apiñaniz, A. Oleaga, P. Venegas, and I. Sáez-Ocáriz, *J. Phys.: Conf. Ser.* **214**(1), 012079 (2010).
- ²⁰Z. Ouyang, L. D. Favro, R. L. Thomas, and X. Han, *AIP Conf. Proc.* **615**(1), 577 (2002).
- ²¹S. X. Zhao, X. Han, L. D. Favro, G. Newaz, and R. L. Thomas, *AIP Conf. Proc.* **1430**(1), 533 (2012).
- ²²O. Obeidat, Q. Yu, and X. Han, *NDT&E Int.* **100**, 11 (2018).
- ²³D. Sharath, M. Menaka, and B. Venkatraman, *Meas. Sci. Technol.* **24**(12), 125205 (2013).
- ²⁴C. Wallbrink, S. A. Wade, and R. Jones, *J. Appl. Phys.* **101**(10), 104907 (2007).